

Foundation Neural-Network Quantum States

Riccardo Rende,^{1,*} Luciano Loris Viteritti,^{2,*} Federico Becca,³
Antonello Scardicchio,^{4,5} Alessandro Laio,^{1,4} and Giuseppe Carleo^{2,†}

¹*International School for Advanced Studies (SISSA), Via Bonomea 265, I-34136 Trieste, Italy*

²*Institute of Physics, École Polytechnique Fédérale de Lausanne (EPFL), CH-1015 Lausanne, Switzerland*

³*Dipartimento di Fisica, Università di Trieste, Strada Costiera 11, I-34151 Trieste, Italy*

⁴*The Abdus Salam ICTP, Strada Costiera 11, 34151 Trieste, Italy*

⁵*INFN, Sezione di Trieste, Via Valerio 2, 34127 Trieste, Italy*

(Dated: June 16, 2025)

Foundation models are highly versatile neural-network architectures capable of processing different data types, such as text and images, and generalizing across various tasks like classification and generation. Inspired by this success, we propose Foundation Neural-Network Quantum States (FNQS) as an integrated paradigm for studying quantum many-body systems. FNQS leverage key principles of foundation models to define variational wave functions based on a single, versatile architecture that processes multimodal inputs, including spin configurations and Hamiltonian physical couplings. Unlike specialized architectures tailored for individual Hamiltonians, FNQS can generalize to physical Hamiltonians beyond those encountered during training, offering a unified framework adaptable to various quantum systems and tasks. FNQS enable the efficient estimation of quantities that are traditionally challenging or computationally intensive to calculate using conventional methods, particularly disorder-averaged observables. Furthermore, the fidelity susceptibility can be easily obtained to uncover quantum phase transitions without prior knowledge of order parameters. These pretrained models can be efficiently fine-tuned for specific quantum systems. The architectures trained in this paper are publicly available at <https://huggingface.co/nqs-models>, along with examples for implementing these neural networks in NetKet.

I. INTRODUCTION

The field of machine learning has undergone a fundamental transformation with the emergence of foundation models [1]. Built upon the Transformer architecture [2], these models have transcended their origins in language tasks [3, 4] to establish new paradigms across domains, from image generation [5] to protein structure prediction [6, 7]. Their efficacy emerges from a profound empirical observation: the scaling of models to hundreds of billions of parameters enables task-agnostic learning that achieves parity with specialized approaches while generating solutions for arbitrary problems defined at inference time [8]. These models exhibit remarkable generalization capabilities, enabling them to adapt to an extensive variety of tasks and domains without requiring task-specific fine-tuning. Another essential feature is their multimodality: they are trained on datasets comprising various formats, including text, images, videos, and audio, allowing them to process and generate outputs that combine these different forms. Foundation models have led to an unprecedented level of homogenization: almost all state-of-the-art natural language processing models are now adapted from a few foundation models. This homogenization produces extremely high leverage since enhancements to foundation models can directly and broadly improve performance across various appli-

cations.

In parallel, the study of quantum many-body systems has been significantly impacted by neural-network architectures employed as variational wave functions [9]. Neural-Network Quantum States (NQS) have emerged as a powerful framework for describing strongly-correlated models with unprecedented accuracy [10–14]. Recent advances in Stochastic Reconfiguration [15–17] have enabled the stable optimization of variational states with millions of parameters [18, 19], while the adaptation of the Transformer architecture for NQS parametrization [20–25] has achieved state-of-the-art performance in challenging systems [19, 21]. Despite this progress, NQS are typically conceived in a system-specific fashion, and studying different Hamiltonians requires significant efforts both in design and numerical optimization strategies.

To address these limitations, we present here Foundation Neural-Network Quantum States (FNQS), a theoretical framework that synthesizes these advances by training neural-network-based variational wave functions capable of integrating as input not only the “standard” basis on which the wave function is represented, but also detailed information about the Hamiltonian (see Fig. 1). Our architecture is designed to achieve three key characteristics of foundation models in the quantum context: multimodality, through the ability to process multiple input types such as spin configurations and physical couplings; homogenization, by applying a single architecture across different Hamiltonians from simple to disordered systems; and generalization to physical Hamiltonians beyond the training dataset.

* These authors contributed equally.

† Correspondence should be addressed to rrende@sissa.it, luciano.viteritti@epfl.ch, and giuseppe.carleo@epfl.ch

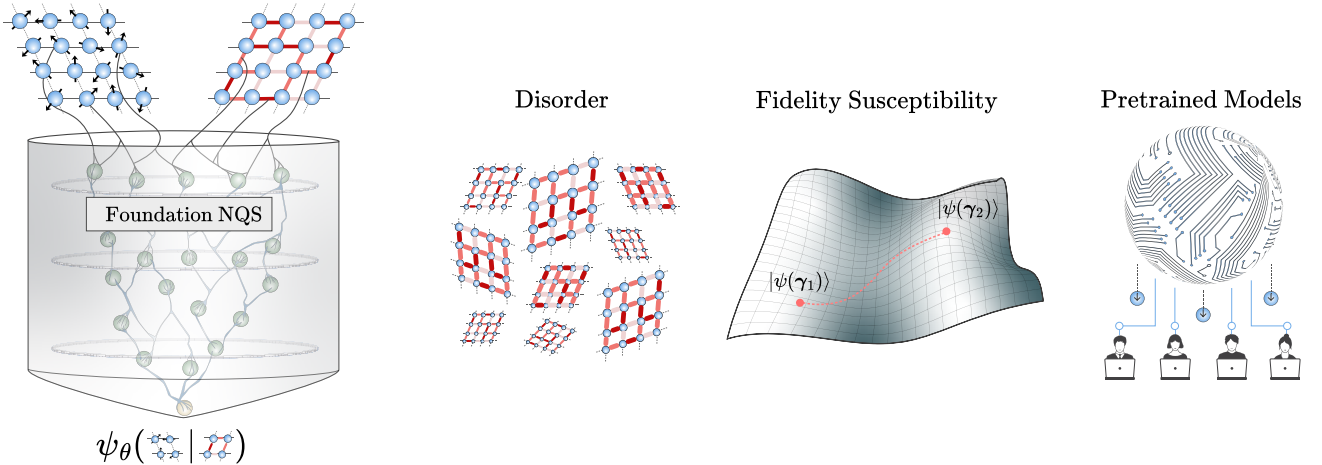


FIG. 1. The first panel from the left shows a pictorial representation of Foundation Neural-Network Quantum States (FNQS), which, unlike traditional NQS, process multimodal inputs by incorporating both physical configurations and Hamiltonian couplings to define a variational wave function amplitude over their joint space. FNQS enable a range of applications, including the efficient simulation of disordered systems (see second panel) and the estimation of the quantum geometric tensor in coupling space, also known as the fidelity susceptibility, for the unsupervised detection of quantum phase transitions (see third panel). Moreover, FNQS combined with the public availability of the architectures allows users to leverage pretrained models to explore coupling regimes beyond those encountered during training (see forth panel).

Previous efforts to construct foundation model-inspired wave functions have been reported in Refs. [26–30]. However, these approaches exhibit several limitations that are addressed in the present work. Specifically, some studies have been constrained to simple physical systems, achieving limited accuracy compared to specialized approaches [26], while others have employed ad hoc optimization strategies for chemical systems [27–29].

In contrast, our work demonstrates applications that are unprecedented in both the diversity and complexity of physical models tackled by a single foundation model. We systematically explore systems of increasing complexity, including two-dimensional frustrated magnets with multiple couplings and disordered systems. This is enabled by the introduction of a suitably designed neural-network wave function based on the Transformer architecture [2, 5], combined with an optimization strategy that extends the Stochastic Reconfiguration method [15, 16] to simultaneously optimize across multiple systems. This generalized optimization procedure is essential to achieve accurate results in the variational Monte Carlo framework.

Most notably, our framework enables simultaneous optimization of wave functions for multiple systems with computational complexity equivalent to single-system optimization, with no performance degradation as the number of systems increases. In addition, the framework enables efficient estimation of the fidelity susceptibility [31], providing rigorous, unsupervised detection of quantum phase transitions without prior knowledge of the order parameters [32, 33]. Refer to Fig. 1 for a pictorial representation of the different applications.

The manuscript proceeds as follows. In Section II, we develop the theoretical framework for simultaneous training of variational wave functions across multiple quantum systems, adapting both Stochastic Reconfiguration for multi-system optimization and the Transformer architecture for multimodal quantum state parametrization. Section III presents systematic validation on the exactly solvable transverse field Ising model in one dimension, followed by an investigation of the J_1 - J_2 - J_3 Heisenberg model on a square lattice through fidelity susceptibility analysis. We conclude with an examination of disordered Hamiltonians, demonstrating the framework's capacity for efficient estimation of disorder-averaged quantities. The hyperparameters of the architectures employed in this work are reported in Section V C of the Appendix.

II. METHODS

The first step in developing foundation models to approximate ground states of quantum many-body Hamiltonians is to establish a theoretical framework that enables training a single NQS to approximate the ground states of multiple systems simultaneously. Consider a family of Hamiltonians, denoted by \hat{H}_γ , where γ is a set of parameters that characterize each specific Hamiltonian, such as the physical couplings. Our goal is to find an approximation of the ground state of the ensemble of Hamiltonians \hat{H}_γ using a variational wave function $|\psi_\theta(\gamma)\rangle$ which explicitly depends on the physical couplings γ and on a shared set of variational parameters θ for all the Hamiltonians. To this end, we define the

following loss function:

$$\mathcal{L}(\theta) = \int d\gamma \mathcal{P}(\gamma) \frac{\langle \psi_\theta(\gamma) | \hat{H}_\gamma | \psi_\theta(\gamma) \rangle}{\langle \psi_\theta(\gamma) | \psi_\theta(\gamma) \rangle}, \quad (1)$$

where $\mathcal{P}(\gamma)$ is a normalized probability density over the couplings, i.e., $\int d\gamma \mathcal{P}(\gamma) = 1$. We denote expectation values with respect to the variational state $|\psi_\theta(\gamma)\rangle$ as $\langle \cdots \rangle_\gamma$. This loss function represents an ensemble average of the energy expectation value $\langle \hat{H}_\gamma \rangle_\gamma$, weighted by the distribution $\mathcal{P}(\gamma)$. For each value of γ , the variational energy $\langle \hat{H}_\gamma \rangle_\gamma$ is bounded from below by the exact ground state energy $E_0(\gamma)$, such that $\langle \hat{H}_\gamma \rangle_\gamma \geq E_0(\gamma)$. Consequently, the loss function in Eq. (1) is bounded as $\mathcal{L}(\theta) \geq \mathcal{L}_0$, where $\mathcal{L}_0 = \int d\gamma \mathcal{P}(\gamma) E_0(\gamma)$ is the average ground state energy over the distribution $\mathcal{P}(\gamma)$.

The loss function in Eq. (1) can equivalently be written in a form amenable for Monte Carlo averages :

$$\mathcal{L}(\theta) = \int d\gamma \mathcal{P}(\gamma) \sum_{\sigma} \frac{|\psi_\theta(\sigma|\gamma)|^2}{\langle \psi_\theta(\gamma) | \psi_\theta(\gamma) \rangle} E_L(\sigma, \gamma). \quad (2)$$

Here, we have introduced the local energy $E_L(\sigma, \gamma) = \langle \sigma | \hat{H}_\gamma | \psi_\theta(\gamma) \rangle / \langle \sigma | \psi_\theta(\gamma) \rangle$ and the wave function $\langle \sigma | \psi_\theta(\gamma) \rangle = \psi_\theta(\sigma|\gamma)$. The latter is parametrized by a neural network, and is the core variational object in our framework. Importantly, the explicit dependence of the many-body wave function amplitude $\psi_\theta(\sigma|\gamma)$ on the Hamiltonian couplings γ is a major difference compared to traditional NQS and aligns with the principles of foundation models, where the capability to handle multiple data modalities, commonly referred to as *multimodality*, plays a central role (see Fig. 1).

The structure of the probability distribution $\mathcal{P}(\gamma)$ depends on the specific application. In disordered systems, a set of couplings $\{\gamma_1, \dots, \gamma_R\}$ can be directly sampled from $\mathcal{P}(\gamma)$, which may have continuous or discrete support. Conversely, in non-disordered systems, the probability distribution can be defined as $\mathcal{P}(\gamma) = 1/\mathcal{R} \sum_{k=1}^{\mathcal{R}} \delta(\gamma - \gamma_k)$, where γ_k denotes the specific instances of the \mathcal{R} Hamiltonians under study.

From a numerical perspective, an expectation value of a generic operator which is written in the form of Eq. (1), can be stochastically estimated using the Variational Monte Carlo framework [17], as discussed in Section V A of the Appendix. In what follows, we denote by M the number of physical configurations used for the stochastic estimation of observables across \mathcal{R} systems. Assuming that the samples are equally distributed across the systems, the number of samples per system is M/\mathcal{R} .

A. Stochastic Reconfiguration for multiple systems

A contribution of this work is the generalization of the Stochastic Reconfiguration (SR) method [15–17] to optimize variational wave functions that minimize loss of

the form given in Eq. (1), thereby enabling the approximation of ground states across an ensemble of Hamiltonians. The key difference from the standard single-system problem is that, in this case, SR is derived as the minimizer of the ensemble-averaged fidelity between the exactly evolved state in imaginary time and the variationally evolved state (see Section V B of Appendix for a detailed derivation).

The SR parameter updates $\delta\theta_\beta$ for $\beta = 1, \dots, P$, with P the total number of parameters, are obtained as

$$\delta\theta = -\eta (\mathcal{S} + \lambda \mathbb{I}_P)^{-1} \mathcal{G}, \quad (3)$$

where η is the learning rate and $\lambda > 0$ is a diagonal shift regularization to ensure the invertibility of the \mathcal{S} matrix (see Section V B of Appendix). On the one hand, the gradient $\mathcal{G}_\alpha = \partial \mathcal{L}(\theta) / \partial \theta_\alpha$ is obtained as $\mathcal{G}_\alpha = \int d\gamma \mathcal{P}(\gamma) G_\alpha(\gamma)$ with

$$G_\alpha(\gamma) = 2\Re \left\{ \langle \hat{H}_\gamma \hat{O}_{\gamma, \alpha} \rangle_\gamma - \langle \hat{H}_\gamma \rangle_\gamma \langle \hat{O}_{\gamma, \alpha} \rangle_\gamma \right\}. \quad (4)$$

Here, $\hat{O}_{\gamma, \alpha}$ is a diagonal operator in the computational basis of the system characterized by couplings γ , whose matrix elements are defined as $\langle \sigma | \hat{O}_{\gamma, \alpha} | \sigma' \rangle = \delta_{\sigma, \sigma'} \partial \text{Log}[\psi_\theta(\sigma|\gamma)] / \partial \theta_\alpha$. On the other hand, the matrix \mathcal{S} in the extended space is $\mathcal{S}_{\alpha\beta} = \int d\gamma \mathcal{P}(\gamma) S_{\alpha\beta}(\gamma)$ with

$$S_{\alpha\beta}(\gamma) = \Re \left\{ \langle \hat{O}_{\gamma, \alpha}^\dagger \hat{O}_{\gamma, \beta} \rangle_\gamma - \langle \hat{O}_{\gamma, \alpha}^\dagger \rangle_\gamma \langle \hat{O}_{\gamma, \beta} \rangle_\gamma \right\}. \quad (5)$$

Importantly, the matrix \mathcal{S} is constructed as an ensemble average of the matrices $S_{\alpha\beta}(\gamma)$ of the individual systems, weighted by the probability distribution $\mathcal{P}(\gamma)$. In the absence of this weighting, \mathcal{S} would reduce to an unweighted integral, leading to large statistical fluctuations and potentially diverging variances in its elements.

For simplicity, we have omitted the dependency of the log-derivative operator $\hat{O}_{\gamma, \alpha}$ and the \mathcal{S} matrix on the variational parameters θ .

B. Foundation Neural-Network architecture

To parametrize the FNQS, we adapt the Vision Transformer (ViT) Ansatz introduced in Ref. [21] to process multimodal inputs, defined by the physical configurations σ and the Hamiltonian couplings γ .

The traditional ViT architecture processes the physical configuration σ in three main steps (see Ref. [21] for a detailed description):

1. *Embedding.* The input configuration σ is split into n patches, where the specific shape of the patches depends on the structure of the lattice and its dimensionality, see for example [20, 21, 23]. Then, the patches are embedded in \mathbb{R}^d through a linear transformation of trainable parameters, defining a sequence of input vectors $(\mathbf{x}_1, \mathbf{x}_2, \dots, \mathbf{x}_n)$.

2. *Transformer Encoder.* The resulting input sequence is processed by a Transformer Encoder, which produces another sequence of vectors $(\mathbf{y}_1, \mathbf{y}_2, \dots, \mathbf{y}_n)$, with $\mathbf{y}_i \in \mathbb{R}^d$ for all i .
3. *Output layer.* These vectors are summed to produce the hidden representation $\mathbf{z} = \sum_{i=1}^n \mathbf{y}_i$, which is finally mapped through a fully-connected layer to a single complex number representing the amplitude corresponding to the input configuration. Only the parameters of this last layer are taken to be complex-valued.

The generalization of the architecture to include as inputs the couplings $\boldsymbol{\gamma}$ is performed by modifying *only* the *Embedding* step described above. In particular, we adopt two different strategies, which cover the systems studied in this work, depending on whether the parameter vector $\boldsymbol{\gamma}$ consists of $O(1)$ or $O(N)$ real numbers, with N indicating the total number of physical degrees of freedom of the model. We stress that the property of having a single, versatile architecture that can be adapted to study physical systems with distinct characteristics, such as a different number of couplings, is a key property of foundation models, also called *homogenization* (see Section I). In the first scenario where the auxiliary parameters are $O(1)$, we concatenate the values of the couplings to each patch of the physical configuration before the linear embedding. Then the usual linear embedding procedure in \mathbb{R}^d is performed. Instead, in the second scenario with $O(N)$ external parameters, we split the vector of the couplings into patches using the same criterion used for the physical configuration. We then use two different embedding matrices to embed the resulting patches of the configuration and of the couplings, generating two sequences of vectors: $(\mathbf{x}_1, \mathbf{x}_2, \dots, \mathbf{x}_n)$ with $\mathbf{x}_i \in \mathbb{R}^{d/2}$ for the physical degrees of freedom and $(\tilde{\mathbf{x}}_1, \tilde{\mathbf{x}}_2, \dots, \tilde{\mathbf{x}}_n)$ with $\tilde{\mathbf{x}}_i \in \mathbb{R}^{d/2}$ for the couplings. The final input to the Transformer is constructed by concatenating the embedding vectors, forming the sequence $(\text{Concat}(\mathbf{x}_1, \tilde{\mathbf{x}}_1), \dots, \text{Concat}(\mathbf{x}_n, \tilde{\mathbf{x}}_n))$, with $\text{Concat}(\mathbf{x}_i, \tilde{\mathbf{x}}_i) \in \mathbb{R}^d$. Notice that after the first layers, the representations of the configurations and of the couplings are mixed by the attention mechanism. The Embedding step can be generalized to any general parameterized Hamiltonian represented as a graph [34].

Regarding the lattice symmetries encoded in the architecture, for non-disordered Hamiltonians we employ a translationally invariant attention mechanism that ensures a variational state invariant under translations among patches [21, 23]. In contrast, for disordered models, we do not impose constraints on the attention mechanism.

C. Generalized Fidelity Susceptibility

A rigorous approach for the unsupervised detection of quantum phase transitions involves measuring the *fidelity susceptibility* [31]. Consider a general system described

by the Hamiltonian $\hat{H}_{\boldsymbol{\gamma}}$ characterized by N_c couplings $\boldsymbol{\gamma} = (\gamma^{(1)}, \gamma^{(2)}, \dots, \gamma^{(N_c)})$. We define the *generalized fidelity susceptibility* as:

$$\chi_{ij}(\boldsymbol{\gamma}) = - \left. \frac{\partial^2 \ln F(\boldsymbol{\gamma}, \epsilon)}{\partial \epsilon_i \partial \epsilon_j} \right|_{\epsilon=0}, \quad (6)$$

where $F(\boldsymbol{\gamma}, \epsilon)$ is the fidelity:

$$F^2(\boldsymbol{\gamma}, \epsilon) = \frac{|\langle \psi_{\theta}(\boldsymbol{\gamma}) | \psi_{\theta}(\boldsymbol{\gamma} + \epsilon) \rangle|^2}{\langle \psi_{\theta}(\boldsymbol{\gamma}) | \psi_{\theta}(\boldsymbol{\gamma}) \rangle \langle \psi_{\theta}(\boldsymbol{\gamma} + \epsilon) | \psi_{\theta}(\boldsymbol{\gamma} + \epsilon) \rangle}. \quad (7)$$

The fidelity measures the overlap between two quantum states on the manifold of the couplings $\boldsymbol{\gamma}$ and it shows a dip in correspondence with a quantum phase transition [31–33]. In the case of a single coupling ($N_c = 1$), the tensor $\chi_{ij}(\boldsymbol{\gamma})$ simplifies to a scalar function, which peaks at the phase transition and diverges in the thermodynamic limit. However, even in this simpler case, computing the fidelity [see Eq. (7)] is challenging, as it becomes an exponentially small quantity with increasing system size. Typically, the fidelity susceptibility is determined using exact diagonalization techniques on small clusters or tensor network-based methods for one-dimensional systems [35]. These methods involve calculating the ground state for each coupling value and applying finite-difference techniques to estimate the second derivative [see Eq. (6)]. Efficient algorithms based on Quantum Monte Carlo methods have been proposed to address this challenge, but they are limited to systems with positive-definite ground states [31]. In this work, we propose an alternative approach that overcomes these limitations. Specifically, we start by rewriting the generalized fidelity susceptibility in Eq. (6) as the quantum geometric tensor with respect to the Hamiltonian couplings $\boldsymbol{\gamma}$ [32, 33], namely:

$$\chi_{ij}(\boldsymbol{\gamma}) = \Re \left\{ \langle \hat{\mathcal{O}}_{\boldsymbol{\gamma},i}^{\dagger} \hat{\mathcal{O}}_{\boldsymbol{\gamma},j} \rangle_{\boldsymbol{\gamma}} - \langle \hat{\mathcal{O}}_{\boldsymbol{\gamma},i}^{\dagger} \rangle_{\boldsymbol{\gamma}} \langle \hat{\mathcal{O}}_{\boldsymbol{\gamma},j} \rangle_{\boldsymbol{\gamma}} \right\}, \quad (8)$$

which is a $N_c \times N_c$ symmetric positive-definite matrix. The operators $\hat{\mathcal{O}}_{\boldsymbol{\gamma},i}$ are diagonal in the computational basis whose matrix elements are defined as $\langle \boldsymbol{\sigma} | \hat{\mathcal{O}}_{\boldsymbol{\gamma},i} | \boldsymbol{\sigma}' \rangle = \delta_{\sigma, \sigma'} \partial \text{Log}[\psi_{\theta}(\boldsymbol{\sigma} | \boldsymbol{\gamma})] / \partial \gamma^{(i)}$, where $\gamma^{(i)}$ is the i -th component of the coupling vector $\boldsymbol{\gamma}$ [refer to Section V G of the Appendix for a derivation of the equivalence between Eq. (8) and Eq. (6)]. By exploiting the multimodal nature of the FNQS wave function, it is possible to compute the derivatives of the amplitudes with respect to the Hamiltonian couplings, a highly non-trivial quantity that is inaccessible for standard variational states optimized on a single value of the couplings. As a result, for FNQS, the quantum geometric tensor in Eq. (8) can be directly computed using automatic differentiation techniques, bypassing the need to explicitly calculate the fidelity [see Eq. (7)].

We emphasize that identifying quantum phase transitions without prior knowledge of order parameters is a challenging task, and existing state-of-the-art methods have notable limitations that hinder their applicability in complicated scenarios. For instance, supervised

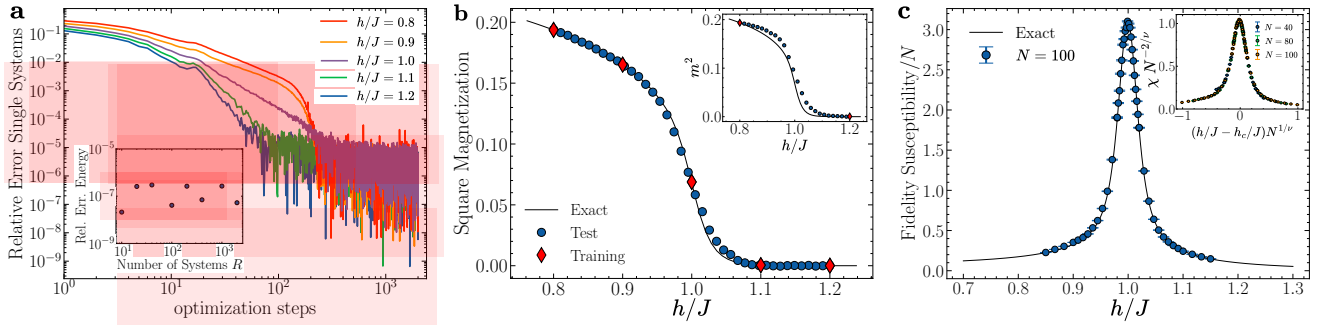


FIG. 2. All the panels refer to the Ising model on a chain [see Eq. (9)]. **Panel a.** Simultaneous ground state energy optimization of $\mathcal{R} = 5$ systems on a chain of $N = 100$ sites, with external fields $h/J = 0.8, 0.9, 1.0, 1.1$ and 1.2 . The relative error with respect to the exact ground state energy of each system is shown as a function of the optimization steps. The inset displays the relative error of the total energy as a function of the number of systems \mathcal{R} , defined by equispaced values of h/J in the interval $h/J \in [0.8, 1.2]$, with a fixed batch size of $M = 10000$. **Panel b.** Square magnetization evaluated with a FNQS trained at $h/J = 0.8, 0.9, 1.0, 1.1$ and 1.2 (red diamonds) and tested on previously *unseen* values of the external field (blue circles). The inset shows the square magnetization predictions of an architecture trained exclusively on $h/J = 0.8$ and 1.2 , evaluated at intermediate external field values. **Panel c.** Fidelity susceptibility per site [see Eq. (8)] as a function of the external field for a FNQS trained on $\mathcal{R} = 6000$ equispaced values of h/J in the interval $h/J \in [0.85, 1.15]$ for a cluster of $N = 100$ sites. The inset shows the data collapse of the same quantity for $N = 40, 80$, and 100 .

approaches [36] require prior knowledge of the different phases, while unsupervised techniques are generally restricted to models with a single physical coupling [37] or rely on quantum tomography, which is typically computationally demanding [38, 39]. All these limitations are overcome by our approach, which extends the computation of fidelity susceptibility [31] to general physical models with multiple couplings.

III. RESULTS

The framework introduced in Section II is general and applicable to quantum systems of different nature. However, in the following, we specialize to spin-1/2 systems.

A. Transverse field Ising chain

In the first place, we test the framework on the one-dimensional Ising model in a transverse field, an established benchmark problem of the field. The system is described by the following Hamiltonian (with periodic boundary conditions):

$$\hat{H} = -J \sum_{i=1}^N \hat{S}_i^z \hat{S}_{i+1}^z - h \sum_{i=1}^N \hat{S}_i^x, \quad (9)$$

where \hat{S}_i^x and \hat{S}_i^z are spin-1/2 operators on site i . The ground-state wave function, for $J, h \geq 0$, is positive definite in the computational basis, with a known exact solution. In this case, the Hamiltonian depends on a single coupling, specifically the external magnetic field h .

In the thermodynamic limit, the ground state exhibits a second-order phase transition at $h/J = 1$, from a ferromagnetic ($h/J < 1$) to a paramagnetic ($h/J > 1$) phase. In finite systems with N sites, the estimation of the critical point can be obtained from the long-range behavior of the spin-spin correlations, that is, $m^2(\gamma) = 1/N \sum_{i=1}^N \langle \hat{S}_{\gamma,i}^z \hat{S}_{\gamma,i+N/2}^z \rangle_{\gamma}$. The quantum phase transition at $h/J = 1$ is in the universality class of the classical two-dimensional Ising model [40].

Here, we first demonstrate the ability to train a FNQS across multiple Hamiltonians, and even across quantum phase transitions. To achieve this, we use the variational Ansatz described in Section II B, training it on a chain of $N = 100$ sites across five different values of the external field ($\mathcal{R} = 5$), including values representative of both the disordered ($h/J = 1.2, 1.1$) and the magnetically ordered phase ($h/J = 0.9, 0.8$), as well as the transition point ($h/J = 1.0$). As shown in Fig. 2a, this single neural network describes all five ground states with high accuracy. The learning speed is only moderately different in the different states. In particular, the state with a value of h/J close to the transition point is the one that converges last. For the same architecture, we systematically vary the value of $\mathcal{R} \in [5, 2000]$, choosing the transverse field equispaced within the interval $h/J \in [0.8, 1.2]$. We keep the total batch size fixed to $M = 10000$, assigning an equal number of samples M/\mathcal{R} across the \mathcal{R} different systems. In the inset of panel (a), we show the relative error of the total energy accuracy as a function of \mathcal{R} . Remarkably, despite the number of systems increasing, the network's performance remains constant, with no observable degradation in accuracy. Crucially, this robustness is achieved at a *computational cost independent of the total number of systems*, as it depends solely on the neural

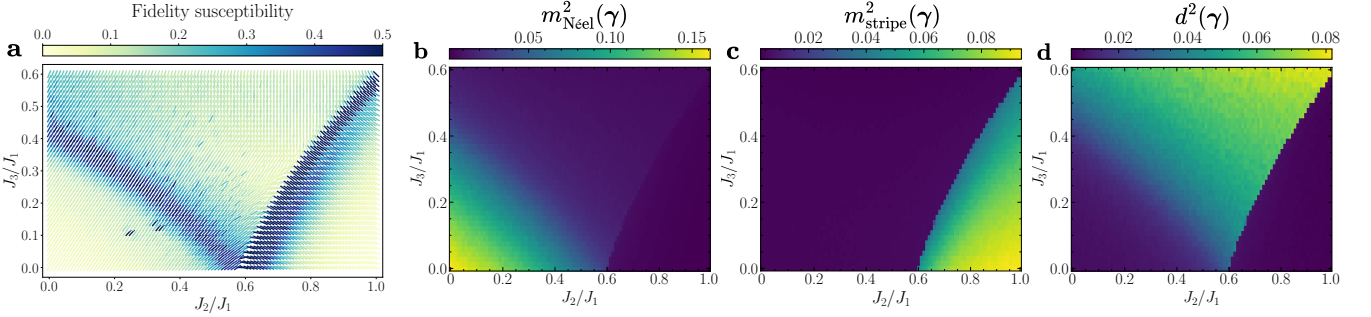


FIG. 3. **Panel a.** Fidelity susceptibility of the J_1 - J_2 - J_3 Heisenberg model on a 10×10 square lattice [see Eq. (10)]. For each point of the phase diagram of the system, we visualize the direction of the leading eigenvector of the quantum geometric tensor $\chi_{ij}(\gamma)$ [see Eq. (8)]. The colour associated to each line is related to corresponding eigenvalue clipped in the interval $[0.0, 0.5]$ for visualization purposes. **Panel b.** The order parameter $m_{\text{Néel}}^2(\gamma)$ characterizing the Néel antiferromagnetic order. **Panel c.** The order parameter $m_{\text{stripe}}^2(\gamma)$ identifying the antiferromagnetic phase with stripe order. **Panel d.** The order parameter $d^2(\gamma)$ probing the valence bond phase. In all panels, the order parameters are computed over a dense grid of $\mathcal{R} = 4000$ uniformly distributed points in the parameter space defined by $J_2/J_1 \in [0, 1.0]$ and $J_3/J_1 \in [0, 0.6]$.

network architecture and the fixed total batch size M . This result is a first illustration of the accuracy, scalability, and computational efficiency of our approach.

Then, we investigate the generalization properties of the FNQS. In panel (b) of Fig. 2, we use the architecture trained with $\mathcal{R} = 5$ and evaluate its performance on external field values not included in the training set. In particular, we compute the square magnetization for other intermediate values of h/J , showing robust generalization capabilities of the network across the entire phase diagram. The inset explores a more restricted scenario in which training is performed using only two points: one in the disordered phase ($h/J = 1.2$) and another in the ordered phase ($h/J = 0.8$). This analysis shows that, even with minimal training data, the network avoids overfitting the ground state at these two points and learns a sufficiently smooth description of the magnetization curve.

Finally, in panel (c) of Fig. 2, we use a FNQS trained on $\mathcal{R} = 6000$ different points equispaced in the interval $h/J \in [0.85, 1.15]$ to calculate the fidelity susceptibility (see Section II C), comparing the FNQS results to the exact solution that is available in this case [35, 41]. In the inset of the same panel, we present a data collapse analysis of the fidelity susceptibility. Specifically, we show the scaled fidelity susceptibility $\chi N^{-2/\nu}$ versus $(h/J - h_c/J)N^{1/\nu}$ according to the scaling laws of Refs. [31, 32, 42, 43]. The data collapses well under $h_c/J = 1.00(1)$ and the critical exponent $\nu = 1.00(2)$ corresponding to the classical two-dimensional Ising universality class [44].

This first benchmark example highlights the ability of the FNQS to interpolate meaningfully between different phases, even when trained on a limited set of Hamiltonians. We attribute this capability to the properties of the ViT architecture employed. In particular, the multi-head attention mechanism could play a crucial role. For example, each attention head can, in principle, specialize in

capturing features associated with distinct phases of the system. Moreover, the all-to-all connectivity intrinsic to the attention mechanism allows the network to flexibly describe long-range correlations, which are essential for accurately describing critical phenomena.

B. J_1 - J_2 - J_3 Heisenberg model

We now proceed to analyzing the J_1 - J_2 - J_3 Heisenberg model on a two-dimensional $L \times L$ square lattice with periodic boundary conditions:

$$\hat{H} = J_1 \sum_{\langle \mathbf{r}, \mathbf{r}' \rangle} \hat{\mathbf{S}}_{\mathbf{r}} \cdot \hat{\mathbf{S}}_{\mathbf{r}'} + J_2 \sum_{\langle\langle \mathbf{r}, \mathbf{r}' \rangle\rangle} \hat{\mathbf{S}}_{\mathbf{r}} \cdot \hat{\mathbf{S}}_{\mathbf{r}'} + J_3 \sum_{\langle\langle\langle \mathbf{r}, \mathbf{r}' \rangle\rangle\rangle} \hat{\mathbf{S}}_{\mathbf{r}} \cdot \hat{\mathbf{S}}_{\mathbf{r}'} , \quad (10)$$

where $\hat{\mathbf{S}}_{\mathbf{r}} = (\hat{S}_{\mathbf{r}}^x, \hat{S}_{\mathbf{r}}^y, \hat{S}_{\mathbf{r}}^z)$ represents the spin-1/2 operator localized at site \mathbf{r} ; in addition, J_1 , J_2 , and J_3 are first-nearest-, second-nearest-, and third-nearest-neighbor antiferromagnetic couplings, respectively. The ground-state properties of this frustrated model have been extensively studied using various numerical and analytical approaches. However, a complete characterization of its phase diagram remains challenging [45–52]. It is well established that antiferromagnetic order dominates in extended regions for $J_1 \gg J_2, J_3$ [with pitch vector $\mathbf{k} = (\pi, \pi)$] and for $J_2 \gg J_1, J_3$ [with pitch vectors $\mathbf{k} = (\pi, 0)$ or $\mathbf{k} = (0, \pi)$]. In contrast, in the intermediate region, frustration suppresses magnetic order, leading to valence-bond solid and, as recently suggested, spin-liquid states [51, 52]. The study of this model using FNQS aims to demonstrate that a single architecture can learn to effectively combine input spin configurations and Hamiltonian couplings, constructing a compact representation that captures and differentiates between distinct phases.

First, we aim for an initial characterization of the phase diagram in a fully unsupervised manner, aiming to dis-

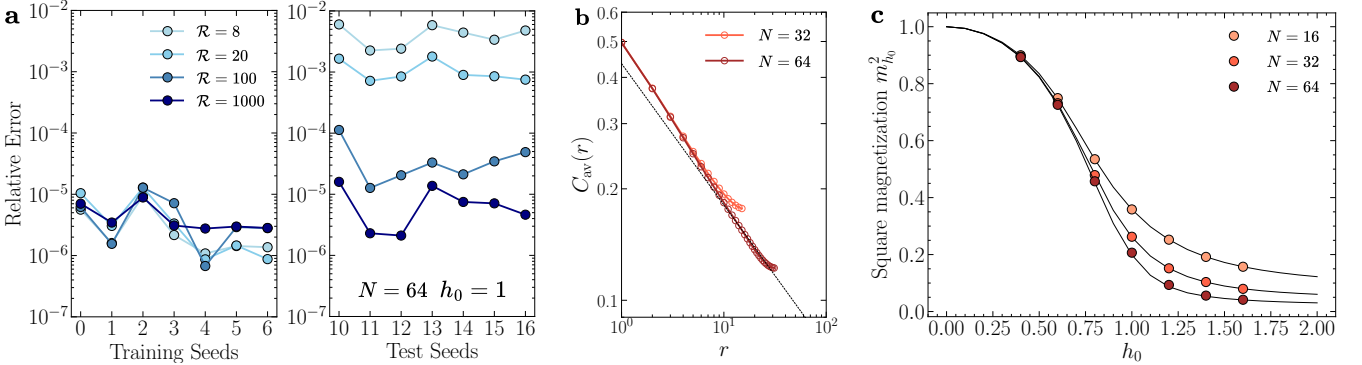


FIG. 4. All the panels refer to the random transverse field Ising model on a chain [see Eq. (13)]. **Panel a.** Relative error of the variational energy on a cluster of $N = 64$ sites, fixing $h_0 = 1.0$ on different train (left) and test (right) disorder realizations increasing the number of systems \mathcal{R} . The integer numbers (seeds) shown on the x-axis label different disorder realizations. Specifically, integers from 0 to 6 correspond to a set of seven different training disorder realizations, while those from 10 to 16 correspond to a set of test realizations. **Panel b.** Spin-spin correlation function averaged over $\mathcal{R} = 1000$ disorder realizations at $h_0 = 1$. The dashed line represent the theoretical power law behaviour with exponent $\eta \approx 0.382$. **Panel c.** Square magnetization $m_{h_0}^2$ as a function of h_0 . At fixed h_0 order parameter is obtained by averaging over $\mathcal{R} = 1000$ different disorder realizations. The numerically exact results are report as comparison with solid lines.

tinguish regions with valence-bond ground states from those with magnetic order using the generalized fidelity susceptibility introduced in Section II C. To this end, we train a FNQS on a 10×10 lattice over a broad region of parameter space, setting a dense grid of $\mathcal{R} = 4000$ evenly spaced points in the plane defined by $J_2/J_1 \in [0, 1.0]$ and $J_3/J_1 \in [0, 0.6]$. Having two couplings J_2/J_1 and J_3/J_1 , the quantum geometric tensor in the couplings space is a 2×2 matrix [see Eq. (8)]. For each point $\gamma = (J_2/J_1, J_3/J_1)$ we diagonalize $\chi_{ij}(\gamma)$ and in Fig. 3a we visualize the direction of the eigenvector corresponding to the maximum eigenvalue using lines, whose colors are associated to the leading eigenvalues and indicate the intensity of maximum variation of the variational wave function. We note that the lines of maximal variation partition the plane into three distinct regions, in agreement with the three different phases identified by the order parameters (see below). Remarkably, within this approach we are able to identify the existence of two phase transitions without any prior knowledge of the physical properties of the system. Furthermore, by analyzing the behavior of the eigenvectors, we can infer the nature of these phase transitions. For example, on the left branch of maximum variation, the eigenvectors exhibit no significant change in direction before and after the transition, which is indicative of a continuous phase transition. In contrast, the right branch shows a pronounced change in the eigenvector directions across the transition, suggesting a first-order phase transition. To the best of our knowledge, this is the first calculation of fidelity susceptibility for a system with more than one coupling. Indeed, without our approach, it would be highly computationally expensive to optimize thousands of systems with different coupling values, using finite difference methods to

estimate the geometric tensor in the couplings space [see Eq. (8)].

To further analyze the physical property of the model, we compute the order parameters in each region of the phase diagram by examining spin-spin and dimer-dimer correlations. Specifically, for fixed values of the Hamiltonian couplings $\gamma = (J_2/J_1, J_3/J_1)$, the antiferromagnetic order is detected by analyzing the spin structure factor

$$C(\mathbf{k}; \gamma) = \sum_{\mathbf{r}} e^{i\mathbf{k} \cdot \mathbf{r}} \langle \hat{\mathbf{S}}_{\gamma,0} \cdot \hat{\mathbf{S}}_{\gamma,\mathbf{r}} \rangle_{\gamma}, \quad (11)$$

where \mathbf{r} runs over all the lattice sites of the square lattice. On the one side, the antiferromagnetic Néel order is detected by measuring $m_{\text{Néel}}^2(\gamma) = C(\pi, \pi; \gamma)/N$ [53, 54] with $N = L^2$. On the other side, the stripe antiferromagnetic order is identified by $m_{\text{stripe}}^2(\gamma) = [C(0, \pi; \gamma) + C(\pi, 0; \gamma)]/(2N)$. In Section V E of the Appendix, we measure these two order parameters by restricting the optimized FNQS to the axis $J_3 = 0$, allowing comparison with other techniques. Furthermore, the valence-bond solid order is detected by the dimer-dimer correlations:

$$D_{\alpha}(\mathbf{r}; \gamma) = 9 \left[\langle \hat{S}_{\gamma,0}^z \hat{S}_{\gamma,\alpha}^z \hat{S}_{\gamma,\mathbf{r}}^z \hat{S}_{\gamma,\mathbf{r}+\alpha}^z \rangle_{\gamma} - \langle \hat{S}_{\gamma,0}^z \hat{S}_{\gamma,\alpha}^z \rangle_{\gamma} \langle \hat{S}_{\gamma,\mathbf{r}}^z \hat{S}_{\gamma,\mathbf{r}+\alpha}^z \rangle_{\gamma} \right], \quad (12)$$

where $\alpha = \hat{\mathbf{x}}, \hat{\mathbf{y}}$. Notice that the previous definition involves only the z component of the spin operators, which is sufficient to detect the dimer order [20, 55]; however, since we consider only one component, we include a factor of 9 in Eq. (12) to account for this [56]. Then, the corresponding structure factor is expressed as $\mathcal{D}_{\alpha}(\mathbf{k}; \gamma) = \sum_{\mathbf{r}} e^{i\mathbf{k} \cdot \mathbf{r}} D_{\alpha}(\mathbf{r}; \gamma)$. The order

parameter to detect the valence-bond order is defined as $d^2(\gamma) = [\mathcal{D}_x(\pi, 0; \gamma) + \mathcal{D}_y(0, \pi; \gamma)] / N$.

In panels (b), (c), and (d) of Fig. 3, we present the order parameters $m_{\text{N\'eel}}^2(\gamma)$, $m_{\text{stripe}}^2(\gamma)$, and $d^2(\gamma)$, which respectively characterize the antiferromagnetic N\'eel, antiferromagnetic stripe, and valence bond solid phases, as functions of the couplings $J_2/J_1 \in [0, 1.0]$ and $J_3/J_1 \in [0, 0.6]$. Comparing the different panels in Fig. 3, we observe a strong correspondence between the phase transition boundaries predicted by fidelity susceptibility and those identified through order parameters. This agreement validates our approach to the unsupervised detection of quantum phase transitions, even in systems with multiple couplings.

C. Random transverse field Ising model

A natural extension of this method involves exploring Hamiltonians with quenched disorder, by optimizing a single FNQS across distinct disorder realizations. Disordered systems are a very vast and ramified topic of research and are at the basis of a theory of complexity [57]. When quantum effects are also included, disordered systems become even more compelling, with recent works highlighting the extension of Anderson localization to a complete ergodicity breaking in interacting quantum systems [58]. These systems are notoriously resilient to numerical approaches [59] and optimizing a single FNQS across many realizations of disorder makes the averaging of the physical quantities, a necessary step for treating disordered systems, much more efficient.

A compelling candidate for study is the random transverse field Ising chain, defined by the following Hamiltonian (assuming periodic boundary conditions):

$$\hat{H} = -J \sum_{i=1}^N \hat{S}_i^z \hat{S}_{i+1}^z - \sum_{i=1}^N h_i \hat{S}_i^x, \quad (13)$$

where h_i is the on-site transverse magnetic field at the i -th site. In the disordered case, h_i varies randomly along the chain, drawn independently and identically from the uniform distribution on the interval $[0, h_0]$. When setting $J = 1/e$, the model exhibits a quantum phase transition between ordered (ferromagnetic) and disordered (paramagnetic) phases for $h_0 = 1$ [60–63]. Although this disordered model cannot be solved analytically due to the lack of translational symmetry, the eigenstates can be found efficiently for each realization of disorder by exploiting the mapping to free fermions [62]. Therefore, relatively large clusters may be considered, just requiring diagonalizations of $N \times N$ matrices [62]. This model is deceptively simple, since for a large region going from the critical point inside the disordered phase, it is affected by Griffiths-McCoy singularities [60, 61].

From a numerical perspective, unlike in previous cases, the coupling distribution $\mathcal{P}(\gamma)$ is a uniform distribution for the N transverse fields h_i in Eq. (13). Consequently,

for each realization of disorder, the number of couplings is equal to the number of sites of the lattice (see Section II B for more details about the strategies to treat this situation). This scenario provides an opportunity to assess the generalization capabilities of the neural network, particularly in its ability to accurately predict properties for new disorder realizations beyond those considered during the training.

In Fig. 4a, we optimize a single FNQS on a cluster of $N = 64$ sites. Training is carried out on \mathcal{R} distinct disorder realizations, sampled by fixing $h_0 = 1$. The left (right) panel presents the relative error of the variational energy for seven different training (test) seeds as a function of the number of training realizations, namely $\mathcal{R} = 8, 20, 100, 1000$, while keeping in all cases the total batch size of spin configurations constant at $M = 10000$. The analysis reveals that increasing \mathcal{R} does not compromise the accuracy on the training seeds. In fact, even with an increase in training points to $\mathcal{R} = 1000$, we achieve highly accurate energy predictions while keeping the number of configurations per system relatively low, specifically $M/\mathcal{R} = 10$. More importantly, the generalization error on the test seeds (disorder realizations not encountered during training) systematically decreases when increasing \mathcal{R} . Notably, for $\mathcal{R} = 1000$, the relative errors of the training and test accuracies show the same order of magnitude, indicating that the FNQS has successfully learned how to combine the disorder couplings with the spin configurations to generate accurate amplitudes in the space of both physical configurations and couplings. We emphasize that the relative error for each disorder realization achieved by the FNQS is comparable to that obtained by training the same architecture on a single disorder realization (not reported here). This highlights the remarkable efficiency of the proposed method.

To assess the ability of FNQS to accurately predict disorder-averaged observables beyond energy, in Fig. 4b we show the average spin-spin correlation function at criticality:

$$C_{\text{av}}(r) = \frac{1}{N} \sum_{i=1}^N \int d\gamma \mathcal{P}(\gamma) \langle \hat{S}_{\gamma,i}^z \hat{S}_{\gamma,i+r}^z \rangle_\gamma. \quad (14)$$

The average correlation function $C_{\text{av}}(r)$ is stochastically estimated by sampling $\mathcal{R} = 1000$ disorder realizations at $h_0 = 1$. Refer to Section V A of the Appendix for further details. We find good agreement with the theoretical critical scaling, characterized by the critical exponent $\eta = (3 - \sqrt{5})/2 \approx 0.382$, which is depicted as a dashed line in Fig. 4b. In Fig. 4c we measure the order parameter of the system as a function of h_0 . In particular, for a fixed value of h_0 , ranging from $h_0 = 0.4$ to $h_0 = 1.6$, we train a single FNQS over $\mathcal{R} = 1000$ distinct disorder realizations sampled for each h_0 . After training, we estimate the square magnetization, defined as $m_{h_0}^2 = 1/N \sum_{r=1}^N C_{\text{av}}(r)$. The variational results are in excellent agreement with numerically exact calculations

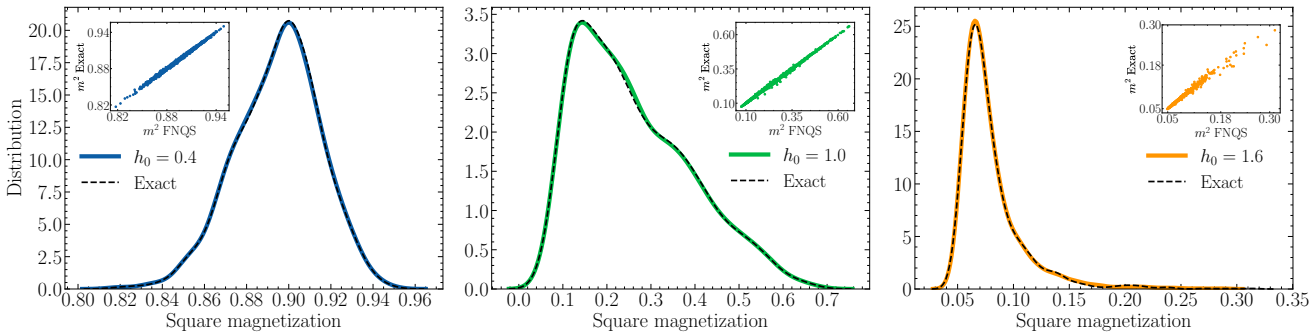


FIG. 5. The distribution of the squared magnetization $m_{h_0}^2$ is analyzed for an FNQS trained on the random transverse field Ising model [see Eq. (13)] with chain length $N = 32$. The FNQS is trained on $\mathcal{R} = 1000$ independent disorder realizations and tested on a separate set of 1000 unseen realizations. The reported distributions correspond to the latter, with results presented for three distinct disorder strengths: $h_0 = 0.4$, $h_0 = 1.0$, and $h_0 = 1.6$. For comparison, numerically exact results are included as black dashed lines. The insets of each panel illustrate the correlation between the exact squared magnetizations and the variational values predicted by the FNQS for unseen disorder realizations.

across different system sizes, namely $N = 16, 32, 64$. Remarkably, achieving similar results with standard methods would require the optimization of 1000 independent simulations for each value of h_0 , highlighting the efficiency and scalability of our approach. To provide a more stringent test of the accuracy of the predicted observables, in Fig. 5 we analyze the distribution of the square magnetization $m_{h_0}^2$ over a set of 1000 *test* disorder realizations *not* encountered during training. The comparison with exact results demonstrates excellent agreement for the different values of $h_0 = 0.4, 1.0$ and 1.6 , capturing not only the regions of high probability density but also the tails of the distributions with remarkable accuracy. In the inset of each panel of Fig. 5, we present correlation plots comparing the exact square magnetization with the FNQS predictions for disorder realizations *not* encountered during training. These plots further highlight the excellent agreement between the predictions and exact results, even for the most extreme and improbable values of the square magnetization.

IV. CONCLUSIONS

We have demonstrated that a single neural-network architecture can be efficiently trained on multiple many-body quantum systems, yielding a variational state that generalizes to previously unseen coupling parameters. This approach enables the use of pre-trained states as starting points for specific investigations [25], similar to current practices in machine learning. To facilitate the adoption of this methodology, we have made FNQS models available through the Hugging Face Hub at <https://huggingface.co/nqs-models>, integrated with the `transformers` library [64] and providing simple interfaces for NetKet [65].

Several research directions emerge from this work.

Specifically, we believe that in the near future, it will be possible to develop FNQS capable of treating all spin models with arbitrary two-body interactions in one and two dimensions. Achieving this ambitious goal will require a step-by-step approach and forms part of a broader long-term research program. Moreover, the extension to fermionic systems in second quantization [66, 67] requires adapting the architecture while maintaining the core methodology. For molecular systems [68], the multimodal structure of FNQS could enable efficient computation of energy derivatives with respect to geometric parameters, providing access to atomic forces and equilibrium configurations. Beyond ground states, these foundation models could potentially facilitate the study of quantum dynamics by introducing explicit time-dependent variational states [69, 70], particularly in large systems where traditional methods become intractable. These developments, combined with the public availability of pre-trained models, represent a step toward making advanced quantum many-body techniques more accessible to the broader physics community.

ACKNOWLEDGMENTS

We thank S. Amodio for preparing Fig. 1. R.R. and L.L.V. acknowledge the CINECA award under the ISCRA initiative for the availability of high-performance computing resources and support. The work of AS was funded by the European Union–NextGenerationEU under the project NRRP “National Centre for HPC, Big Data and Quantum Computing (HPC)” CN00000013 (CUP D43C22001240001) [MUR Decree n. 341–15/03/2022] – Cascade Call launched by SPOKE 10 POLIMI: “CQEBC” project, and from the National Recovery and Resilience Plan (NRRP), Mission 4 Component 2 Investment 1.3 funded by the European

Union NextGenerationEU, National Quantum Science and Technology Institute (NQSTI), PE00000023, Concession Decree No. 1564 of 11.10.2022 adopted by the Italian Ministry of Research, CUP J97G22000390007.

V. APPENDIX

A. Expectation values

Given a set of operators \hat{A}_γ parametrized by the couplings γ , its ensemble average over the distribution $\mathcal{P}(\gamma)$ is expressed as:

$$A(\theta) = \int d\gamma \mathcal{P}(\gamma) \frac{\langle \psi_\theta(\gamma) | \hat{A}_\gamma | \psi_\theta(\gamma) \rangle}{\langle \psi_\theta(\gamma) | \psi_\theta(\gamma) \rangle}. \quad (15)$$

This expectation value can be stochastically evaluated using a set of \mathcal{R} couplings $\{\gamma_1, \dots, \gamma_{\mathcal{R}}\}$ sampled from the probability distribution $\mathcal{P}(\gamma)$ as:

$$A(\theta) \approx \frac{1}{\mathcal{R}} \sum_{k=1}^{\mathcal{R}} \frac{\langle \psi_\theta(\gamma_k) | \hat{A}_{\gamma_k} | \psi_\theta(\gamma_k) \rangle}{\langle \psi_\theta(\gamma_k) | \psi_\theta(\gamma_k) \rangle}. \quad (16)$$

Each term in the sum of Eq. (16) can be rewritten as:

$$\frac{\langle \psi_\theta(\gamma_k) | \hat{A}_{\gamma_k} | \psi_\theta(\gamma_k) \rangle}{\langle \psi_\theta(\gamma_k) | \psi_\theta(\gamma_k) \rangle} = \sum_{\sigma} p_\theta(\sigma | \gamma_k) \frac{\langle \sigma | \hat{A}_{\gamma_k} | \psi_\theta(\gamma_k) \rangle}{\langle \sigma | \psi_\theta(\gamma_k) \rangle}. \quad (17)$$

where we have defined the probability distribution $p_\theta(\sigma | \gamma_k) = |\psi_\theta(\sigma | \gamma_k)|^2 / \langle \psi_\theta(\gamma_k) | \psi_\theta(\gamma_k) \rangle$. In the Variational Monte Carlo (VMC) framework [17], this expectation value can be further estimated stochastically over a set of M_k physical configurations $\{\sigma_1, \dots, \sigma_{M_k}\}$ sampled according to the probability distribution $p_\theta(\sigma | \gamma_k)$:

$$\bar{A}_k = \frac{1}{M_k} \sum_{j=1}^{M_k} \frac{\langle \sigma_j | \hat{A}_{\gamma_k} | \psi_\theta(\gamma_k) \rangle}{\langle \sigma_j | \psi_\theta(\gamma_k) \rangle}. \quad (18)$$

In the calculations performed in this work, we set an equal number of samples for each system, $M_k = M/\mathcal{R}$, independent of k , where M is the total number of samples in the extended space of all systems. See to Ref. [17] for further details on the VMC framework.

B. Derivation of the Stochastic Reconfiguration equation for multiple systems

To derive the Stochastic Reconfiguration (SR) equations for multiple systems, we employ the paradigm of the Time-Dependent Variational Principle (TDVP) [71]. Consider a system characterized by coupling parameters γ . We begin by defining the fidelity between the state evolved in imaginary time under the exact Hamiltonian for a time-step ε , namely $e^{-\varepsilon \hat{H}_\gamma} |\psi_{\theta(\tau)}(\gamma)\rangle$, and the corresponding variationally evolved state $|\psi_{\theta(\tau)+\varepsilon\dot{\theta}(\tau)}(\gamma)\rangle$.

Here, $\dot{\theta}_\alpha(\tau)$ denotes the derivative of the α -th variational parameter with respect to imaginary time τ , with $\alpha = 1, \dots, P$ and P the total number of parameters. For simplicity in the notation, in the following, we omit the explicit time dependence of the variational parameters.

The fidelity is then given by:

$$f^2(\gamma) = \frac{|\langle \psi_\theta(\gamma) | e^{-\varepsilon \hat{H}_\gamma} | \psi_{\theta+\varepsilon\dot{\theta}}(\gamma) \rangle|^2}{\langle \psi_\theta(\gamma) | e^{-\varepsilon \hat{H}_\gamma} | \psi_\theta(\gamma) \rangle \langle \psi_{\theta+\varepsilon\dot{\theta}}(\gamma) | \psi_{\theta+\varepsilon\dot{\theta}}(\gamma) \rangle}. \quad (19)$$

Expanding this expression, assuming real-valued variational parameters and neglecting third-order contributions in ε , we obtain:

$$f^2(\gamma) \approx 1 - \varepsilon^2 \left[\dot{\theta}^T \mathbf{G}(\gamma) + \dot{\theta}^T \mathcal{S}(\gamma) \dot{\theta} + \text{Var}(\hat{H}_\gamma) \right]. \quad (20)$$

Here, $\mathbf{G}_\alpha(\gamma)$ is the gradient of the energy defined in Eq. (4) and $\mathcal{S}_{\alpha,\beta}(\gamma)$ is the real part of the quantum geometric tensor defined in Eq. (5). To extend this to an ensemble of systems, we define the global fidelity as the ensemble average of the fidelity over the distribution $\mathcal{P}(\gamma)$ as $\mathcal{F}^2 = \int d\gamma \mathcal{P}(\gamma) f^2(\gamma)$. Substituting Eq. (20) into the previous expression yields

$$\mathcal{F}^2 \approx 1 - \varepsilon^2 \left[\dot{\theta}^T \mathcal{G}(\gamma) + \dot{\theta}^T \mathcal{S}(\gamma) \dot{\theta} + \int d\gamma \mathcal{P}(\gamma) \text{Var}(\hat{H}_\gamma) \right], \quad (21)$$

where the ensemble-averaged quantities are defined as $\mathcal{G}_\alpha = \int d\gamma \mathcal{P}(\gamma) \mathbf{G}_\alpha(\gamma)$ and $\mathcal{S}_{\alpha,\beta} = \int d\gamma \mathcal{P}(\gamma) \mathcal{S}_{\alpha,\beta}(\gamma)$ [see Section II A].

The TDVP equations for the ensemble are obtained by maximizing the global fidelity in Eq. (21) with respect to $\dot{\theta}$, leading to the linear system $\mathcal{S} \dot{\theta} = -\frac{1}{2} \mathcal{G}$. This differential equation can then be integrated numerically. In ground-state applications, it is common to employ the simple Euler scheme, which approximates the time derivative as $\dot{\theta}_\alpha(\tau) \approx [\theta(\tau + \eta) - \theta(\tau)] / \eta$. Here, τ denotes the imaginary time parameterizing the dynamics, and η is the integration time step used to discretize the evolution. Based on these results, the SR updates are conventionally defined by removing the factor of $1/2$ [72, 73] leading to $\delta\theta = -\eta \mathcal{S}^{-1} \mathcal{G}$, where we have defined $\delta\theta_\alpha = \theta_\alpha(\tau + \eta) - \theta_\alpha(\tau)$. It is important to consider that the matrix \mathcal{S} may possess extremely small or even negligible eigenvalues. As a result, directly computing its inverse can lead to numerical instabilities [17]. To mitigate these potential issues, we adopt a regularized update scheme of the form:

$$\delta\theta = -\eta (\mathcal{S} + \lambda \mathbb{I}_P)^{-1} \mathcal{G}, \quad (22)$$

where η acts as a learning rate controlling the update magnitude during the optimization process, and $\lambda > 0$ is a regularization parameter introduced to ensure the invertibility and numerical stability of the matrix \mathcal{S} matrix [17, 19]. The resulting updates are also reported in Eq. (3) of Section II A.

	Architecture				Optimization			
	n_l	n_h	d	b	M	N_{opt}	η	λ
Ising trasverse field	6	12	72	4	10000	2000	0.03	10^{-4}
J_1 - J_2 - J_3 Heisenberg	8	12	72	2×2	16000	3500	0.03	5×10^{-4}
Random transverse field Ising	6	12	72	4	10000	4000	0.03	10^{-4}

TABLE I. This table presents the hyperparameters of the FNQS wave function used to simulate different systems. The *Architecture* columns specify the number of layers n_l , number of heads n_h , embedding dimension d , and patch size b . The *Optimization* columns list the hyperparameters for the Stochastic Reconfiguration method (see Section II A), including the total batch size M , the number of optimization steps N_{opt} , the learning rate η , and the diagonal shift regularization λ .

C. Hyperparameters

In Table I we provide the hyperparameters of the FNQS architecture and the optimization protocol used to study the various systems. See Refs. [17, 19, 21] for more details about the role of the different hyperparameters.

D. Systematic energy improvement

In this section, we systematically increase the expressivity of the FNQS by varying the number of parameters and assess the resulting performance using the V-score [74], a metric known to correlate with the accuracy of the wave function. The V-score for the system \hat{H}_γ is defined as

$$\text{V-score}(\gamma) = N \frac{\langle H_\gamma^2 \rangle_\gamma - \langle H_\gamma \rangle_\gamma^2}{\langle H_\gamma \rangle_\gamma^2}. \quad (23)$$

A key advantage of the V-score is that it can be computed without requiring access to exact reference energies, making it particularly suitable for benchmarking variational methods on large systems [74].

The goal of this analysis is to demonstrate that the accuracy of the FNQS can be systematically improved by increasing the size of the neural network, which we control by adjusting the number of layers. We carry out this study on the J_1 - J_2 Heisenberg model on the square lattice, a widely established benchmark, obtained by setting $J_3 = 0$ in Eq. (10). Specifically, we consider system sizes ranging from $L = 6$ to $L = 12$, and vary the number of layers from $n_l = 2$ to $n_l = 8$. The FNQS is optimized across $\mathcal{R} = 1000$ coupling values, uniformly sampled in the interval $J_2/J_1 \in [0, 1]$. Importantly, for a fixed network architecture and total number of Monte Carlo samples M , the computational cost of each simulation remains independent of \mathcal{R} . Additionally, while the computational complexity of the ViT scales quadratically with the input sequence length, this cost can be mitigated through various strategies [21].

After optimizing the FNQS, we focus on two representative values of the frustration ratio: $J_2/J_1 = 0.5$ and $J_2/J_1 = 0.2$. In the left panel of Fig. 6, we present results for $J_2/J_1 = 0.5$, a highly frustrated point in the phase

diagram [10]. At this value, high-precision ground-state energy estimates obtained via zero-variance extrapolation are available for system sizes beyond $L = 6$ [18, 75], enabling us to validate the correlation between the relative energy error and the V-score, as shown in the inset of the left panel of Fig. 6. In the right panel of Fig. 6, we report the V-score for $J_2/J_1 = 0.2$, a less frustrated point closer to the unfrustrated Heisenberg model. Due to the reduced complexity of the ground state in this region, the V-scores are systematically lower compared to the highly frustrated case at $J_2/J_1 = 0.5$. By analyzing system sizes up to $N = 144$ spins for both frustration ratios, we find that the V-score, and thus the accuracy, systematically improves when increasing the number of parameters in the network, while marginally deteriorating with the system size for a fixed architecture. These results highlight the size-consistency of the ViT parametrization of the FNQS, even when the model is simultaneously optimized across multiple systems. We remark that further improvements in accuracy are achievable by explicitly incorporating the symmetries of the underlying Hamiltonian, although this lies beyond the scope of the present analysis.

E. Structure factor for $J_3/J_1 = 0$

In this section, we evaluate the accuracy of the FNQS trained within the parameter region $J_2/J_1 \in [0, 1.0]$ and $J_3/J_1 \in [0, 0.6]$ of the J_1 - J_2 - J_3 Heisenberg model (see Section III B), focusing on the line $J_3/J_1 = 0$.

The left panel of Fig. 7 shows the results for a 6×6 lattice, where we compute the Néel and stripe order parameters, respectively $m_{\text{Néel}}^2$ and m_{stripe}^2 , as defined in Section III B. Our FNQS predictions are in excellent agreement with exact diagonalization results, demonstrating the reliability of the FNQS architecture.

In the right panel of Fig. 7, we extend this analysis to a 10×10 lattice, using the same setup as in Section III B. Since exact diagonalization is infeasible at this system size, we benchmark FNQS predictions against Quantum Monte Carlo (QMC) data at the unfrustrated point $J_2/J_1 = 0.0$ [54] and against results from a state-of-the-art ViT architecture trained from scratch at $J_2/J_1 = 0.5$ [19].

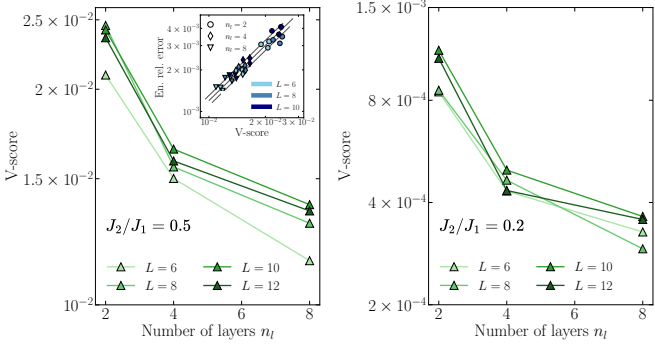


FIG. 6. V-score for the J_1 – J_2 Heisenberg model on the square lattice as a function of the number of layers n_l of the FNQS, for increasing the system size from $L = 6$ to $L = 12$. The left panel shows results for the highly frustrated point $J_2/J_1 = 0.5$, while the right panel corresponds to the less frustrated point $J_2/J_1 = 0.2$. The inset in the left panel displays the correlation between the V-score and the relative energy error at $J_2/J_1 = 0.5$ for system sizes $L = 6$ to $L = 10$. Reference energies for $L = 8$ and $L = 10$ are obtained via zero-variance extrapolation from Refs. [18, 75].

F. Out of distribution generalization

In this section, we investigate whether a FNQS trained on a restricted coupling domain can generalize to couplings outside this domain, namely for $\gamma \notin \text{Dom}\{\mathcal{P}(\gamma)\}$. In general, we do not expect this type of out-of-distribution generalization to succeed, as in any other machine learning approach. Nonetheless, we report here an example where this type of unconventional generalization is effective with some limitations.

Specifically, we consider the following Hamiltonian defined by generalizing the J_1 – J_2 Heisenberg model on a square lattice (with periodic boundary conditions) [10, 75]:

$$\hat{H} = J_1 \sum_i \left(\hat{\mathbf{S}}_i \cdot \hat{\mathbf{S}}_{i+\hat{y}} + \hat{\mathbf{S}}_i \cdot \hat{\mathbf{S}}_{i+\hat{x}} \right) + \sum_i \left(J_{2L} \hat{\mathbf{S}}_i \cdot \hat{\mathbf{S}}_{i+\hat{x}+\hat{y}} + J_{2R} \hat{\mathbf{S}}_i \cdot \hat{\mathbf{S}}_{i+\hat{x}-\hat{y}} \right) \quad (24)$$

which depends on two distinct couplings, J_{2L}/J_1 and J_{2R}/J_1 . When $J_{2L} = J_{2R} = 0$, the model reduces to the unfrustrated Heisenberg model on a square lattice, whose ground state exhibits antiferromagnetic order [54]. Increasing J_{2L} introduces frustration exclusively along the left diagonals of the square lattice, while increasing J_{2R} does so along the right diagonals (see Fig. 8a). In the limiting cases where either $J_{2L} \neq 0$ and $J_{2R} = 0$, or vice versa, the model in Eq. (24) corresponds to the Heisenberg model on the anisotropic triangular lattice [76–78].

To probe the generalization capability of the FNQS model, we design the following experiment (illustrated in Fig. 8a): the architecture is trained solely on Hamilton-

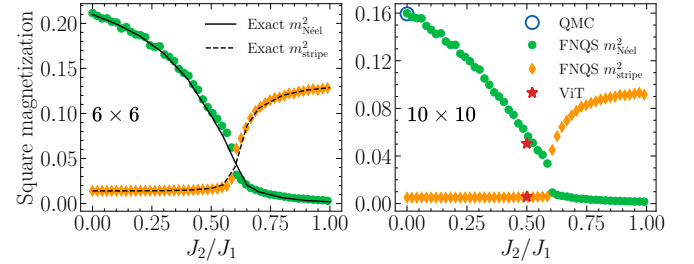


FIG. 7. Square magnetization corresponding to the Néel ($m_{\text{Néel}}^2$) and stripe (m_{stripe}^2) order as a function of the frustration ratio J_2/J_1 . The left panel corresponds to a 6×6 lattice, in which the FNQS results at $J_3/J_1 = 0$ are compared with exact diagonalization calculations (solid and dashed black lines). The right panel corresponds to a 10×10 lattice, in which the variational results are compared with Quantum Monte Carlo (QMC, blue circles) at $J_2/J_1 = 0$, and with Vision Transformer architecture (ViT, red stars) at $J_2/J_1 = 0.5$.

nians where frustration is present on only one diagonal at a time and then evaluated on Hamiltonians in which both diagonals are simultaneously frustrated. Specifically, the training data are sampled from a coupling distribution $\mathcal{P}(\gamma)$ defined exclusively on points of the form $(J_{2L}/J_1, 0)$ or $(0, J_{2R}/J_1)$, where only one of the two next-nearest-neighbor couplings is active, with J_{2L} and J_{2R} harvested from a uniform distribution defined on the interval $[0.0, 0.6]$. We then assess whether the resulting model can generalize to coupling configurations with $J_{2L} = J_{2R}$, which recover the J_1 – J_2 Heisenberg model on a square lattice [10, 75], where frustration is introduced symmetrically along both diagonals. Importantly, such test points lie outside the support of the training distribution $\mathcal{P}(\gamma)$, challenging the model's ability to extrapolate beyond its training regime. In Fig. 8b, we consider a 6×6 lattice and plot the spin–spin correlation function at two in-distribution points, $(J_{2L}/J_1, J_{2R}/J_1) = (0.0, 0.3)$ and $(0.3, 0.0)$, as well as at the out-of-distribution point $(0.3, 0.3)$. Remarkably, the FNQS accurately captures the enhanced frustration in the latter case, producing correlation functions that have lower amplitudes than in the case with only one frustrated diagonal at a time, and in close agreement with exact results. This demonstrates the model's surprising ability to generalize beyond the support of the training distribution. However, it is important to emphasize that the accuracy of such generalization decreases as the distance from the training axis ($J_{2L} = 0$ or $J_{2R} = 0$) increases. Specifically, along the diagonal direction ($J_{2L} = J_{2R}$), the relative error on the ground-state energy remains very small in the Néel antiferromagnetic phase of the J_1 – J_2 Heisenberg model, on the order of 10^{-5} for $J_2 = 0.1$, 10^{-4} for $J_2 = 0.3$, but increases substantially to order 10^{-2} for $J_2 = 0.5$ and 10^{-1} for $J_2 = 0.6$. This degradation in generalization performance is illustrated in Fig. 8c, which shows the behavior of the Néel antiferromagnetic order parameter

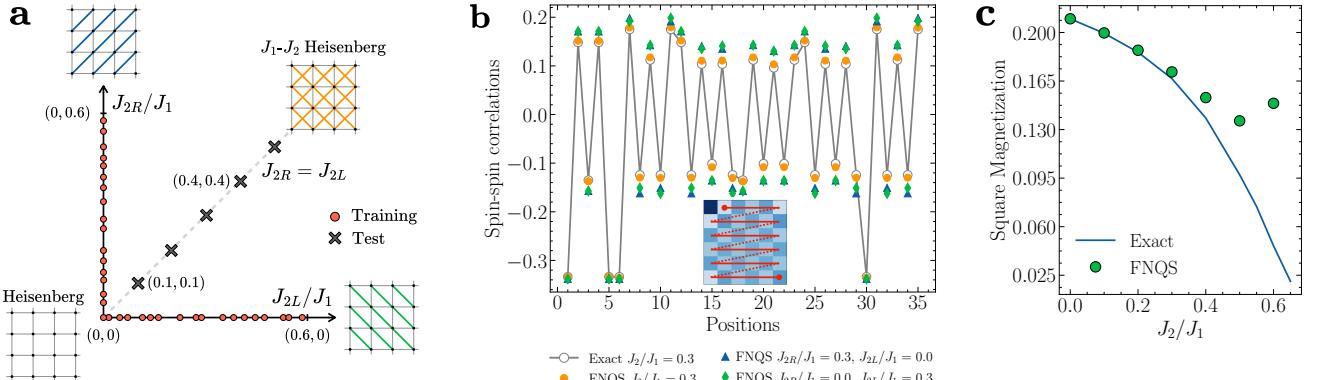


FIG. 8. **Panel a:** Generalized J_1 – J_2 Heisenberg model on a square lattice, with two couplings, J_{2L}/J_1 and J_{2R}/J_1 . When $J_{2L} = J_{2R}$, the model reduces to the standard J_1 – J_2 Heisenberg model. The FNQS is trained on configurations with frustration on only one diagonal and tested on configurations where both diagonals are frustrated. **Panel b:** Spin–spin correlation function on a 6×6 lattice of a FNQS trained on $\mathcal{R} = 1000$ different realizations of frustration affecting only one of the two diagonals of a square lattice (see Fig. 8 for a schematic representation). The model is tested on two in-distribution points $(J_{2L}/J_1, J_{2R}/J_1) = (0.0, 0.3)$ and $(0.3, 0.0)$, and on the out-of-distribution point $(J_{2L}/J_1, J_{2R}/J_1) = (0.3, 0.3)$, where both diagonals are frustrated. For reference, the exact results of the J_1 – J_2 Heisenberg model at $J_2 = 0.3$ are also shown. Inset: The red line shows how the spin–spin correlations are ordered in the panel (b). **Panel c:** Out-of-distribution generalization of the square magnetization associated with Néel antiferromagnetic order for the FNQS (green circles) as a function of the frustration ratio J_2/J_1 on a 6×6 cluster. Exact results (blue line) are shown for reference.

$m^2 = S(\pi, \pi)/N$, where $S(\mathbf{k}) = \sum_{\mathbf{r}} e^{i\mathbf{k} \cdot \mathbf{r}} \langle \hat{\mathbf{S}}_0 \cdot \hat{\mathbf{S}}_{\mathbf{r}} \rangle$ is the spin structure factor and N is the total number of sites in the J_1 – J_2 Heisenberg model ($J_{2L} = J_{2R}$).

G. Derivation of the generalized fidelity susceptibility

The fidelity $F^2(\gamma, \varepsilon)$ can be expanded in a Taylor series around $\varepsilon = 0$ as

$$F^2(\gamma, \varepsilon) = 1 - \sum_{i,j=1}^{N_c} \varepsilon_i \varepsilon_j \chi_{ij}(\gamma) + O(|\varepsilon|^3), \quad (25)$$

where N_c denotes the number of couplings.

The leading non-zero contribution to fidelity is given

by the real part of the *quantum geometric tensor* with respect to couplings γ [32, 33], as defined in Eq. (8).

Taking the logarithm of Eq. (25), we obtain

$$\ln[F(\gamma, \varepsilon)] = -\frac{1}{2} \sum_{i,j=1}^{N_c} \varepsilon_i \varepsilon_j \chi_{ij}(\gamma) + O(|\varepsilon|^3). \quad (26)$$

Differentiating twice with respect to ε , we find the Hessian matrix

$$\frac{\partial^2 \ln F(\gamma, \varepsilon)}{\partial \varepsilon_i \partial \varepsilon_j} = -\chi_{ij}(\gamma) + O(|\varepsilon|). \quad (27)$$

At the end, evaluating Eq. (27) at $\varepsilon = 0$ yields the *generalized fidelity susceptibility*, as defined in Eq. (6).

-
- [1] R. Bommasani, D. A. Hudson, E. Adeli, R. Altman, S. Arora, S. von Arx, M. S. Bernstein, J. Bohg, A. Bosselut, E. Brunskill, E. Brynjolfsson, *et al.*, *On the opportunities and risks of foundation models* (2022), arXiv:2108.07258 [cs.LG].
- [2] A. Vaswani, N. Shazeer, N. Parmar, J. Uszkoreit, L. Jones, A. N. Gomez, L. u. Kaiser, and I. Polosukhin, Attention is all you need, in *Advances in Neural Information Processing Systems*, Vol. 30, edited by I. Guyon, U. V. Luxburg, S. Bengio, H. Wallach, R. Fergus, S. Vishwanathan, and R. Garnett (Curran Associates, Inc., 2017).
- [3] J. Devlin, M.-W. Chang, K. Lee, and K. Toutanova, BERT: Pre-training of deep bidirectional transformers for language understanding, in *Proceedings of the 2019 Conference of the North American Chapter of the Association for Computational Linguistics: Human Language Technologies, Volume 1 (Long and Short Papers)*, edited by J. Burstein, C. Doran, and T. Solorio (Association for Computational Linguistics, Minneapolis, Minnesota, 2019) pp. 4171–4186.
- [4] J. Achiam, S. Adler, S. Agarwal, L. Ahmad, I. Akkaya, F. L. Aleman, D. Almeida, J. Altenschmidt, S. Altman, S. Anadkat, *et al.*, Gpt-4 technical report, arXiv preprint arXiv:2303.08774 (2023).
- [5] A. Dosovitskiy, L. Beyer, A. Kolesnikov, D. Weissenborn,

- X. Zhai, T. Unterthiner, M. Dehghani, M. Minderer, G. Heigold, S. Gelly, J. Uszkoreit, and N. Houlsby, [An image is worth 16x16 words: Transformers for image recognition at scale](#) (2021), [arXiv:2010.11929 \[cs.CV\]](#).
- [6] A. Rives, J. Meier, T. Sercu, S. Goyal, Z. Lin, J. Liu, D. Guo, M. Ott, C. L. Zitnick, J. Ma, and R. Fergus, Biological structure and function emerge from scaling unsupervised learning to 250 million protein sequences, *Proceedings of the National Academy of Sciences* **118**, e2016239118 (2021), <https://www.pnas.org/doi/pdf/10.1073/pnas.2016239118>.
- [7] J. M. Jumper, R. Evans, A. Pritzel, T. Green, M. Figurnov, O. Ronneberger, K. Tunyasuvunakool, R. Bates, A. Žídek, A. Potapenko, A. Bridgland, C. Meyer, S. A. A. Kohl, A. Ballard, A. Cowie, B. Romera-Paredes, S. Nikolov, R. Jain, J. Adler, T. Back, S. Petersen, D. Reiman, E. Clancy, M. Zielinski, M. Steinegger, M. Pacholska, T. Berghammer, S. Bodenstein, D. Silver, O. Vinyals, A. W. Senior, K. Kavukcuoglu, P. Kohli, and D. Hassabis, Highly accurate protein structure prediction with alphafold, *Nature* **596**, 583 (2021).
- [8] T. Brown, B. Mann, N. Ryder, M. Subbiah, J. D. Kaplan, P. Dhariwal, A. Neelakantan, P. Shyam, G. Sastry, A. Askell, S. Agarwal, A. Herbert-Voss, G. Krueger, T. Henighan, R. Child, A. Ramesh, D. Ziegler, J. Wu, C. Winter, C. Hesse, M. Chen, E. Sigler, M. Litwin, S. Gray, B. Chess, J. Clark, C. Berner, S. McCandlish, A. Radford, I. Sutskever, and D. Amodei, Language models are few-shot learners, in *Advances in Neural Information Processing Systems*, Vol. 33, edited by H. Larochelle, M. Ranzato, R. Hadsell, M. Balcan, and H. Lin (Curran Associates, Inc., 2020) pp. 1877–1901.
- [9] G. Carleo and M. Troyer, Solving the quantum many-body problem with artificial neural networks, *Science* **355**, 602 (2017).
- [10] Y. Nomura and M. Imada, Dirac-type nodal spin liquid revealed by refined quantum many-body solver using neural-network wave function, correlation ratio, and level spectroscopy, *Phys. Rev. X* **11**, 031034 (2021).
- [11] J. Robledo Moreno, G. Carleo, A. Georges, and J. Stokes, Fermionic wave functions from neural-network constrained hidden states, *Proceedings of the National Academy of Sciences* **119**, [10.1073/pnas.2122059119](#) (2022).
- [12] C. Roth, A. Szabó, and A. H. MacDonald, High-accuracy variational monte carlo for frustrated magnets with deep neural networks, *Phys. Rev. B* **108**, 054410 (2023).
- [13] D. Pfau, J. S. Spencer, A. G. D. G. Matthews, and W. M. C. Foulkes, Ab initio solution of the many-electron schrödinger equation with deep neural networks, *Phys. Rev. Res.* **2**, 033429 (2020).
- [14] D. Luo and B. K. Clark, Backflow transformations via neural networks for quantum many-body wave functions, *Physical Review Letters* **122**, [10.1103/physrevlett.122.226401](#) (2019).
- [15] S. Sorella, Green function monte carlo with stochastic reconfiguration, *Phys. Rev. Lett.* **80**, 4558 (1998).
- [16] S. Sorella, Wave function optimization in the variational monte carlo method, *Phys. Rev. B* **71**, 241103 (2005).
- [17] F. Becca and S. Sorella, *Quantum Monte Carlo Approaches for Correlated Systems* (Cambridge University Press, 2017).
- [18] A. Chen and M. Heyl, Empowering deep neural quantum states through efficient optimization, *Nature Physics* **20**, 1476 (2024).
- [19] R. Rende, L. L. Viteritti, L. Bardone, F. Becca, and S. Goldt, A simple linear algebra identity to optimize large-scale neural network quantum states, *Communications Physics* **7**, [10.1038/s42005-024-01732-4](#) (2024).
- [20] L. L. Viteritti, R. Rende, and F. Becca, Transformer variational wave functions for frustrated quantum spin systems, *Phys. Rev. Lett.* **130**, 236401 (2023).
- [21] L. L. Viteritti, R. Rende, A. Parola, S. Goldt, and F. Becca, Transformer wave function for two dimensional frustrated magnets: emergence of a spin-liquid phase in the shastry-sutherland model (2024), [arXiv:2311.16889 \[cond-mat.str-el\]](#).
- [22] K. Sprague and S. Czischek, Variational monte carlo with large patched transformers, *Communications Physics* **7**, 90 (2024).
- [23] R. Rende and L. L. Viteritti, Are queries and keys always relevant? a case study on transformer wave functions, *Machine Learning: Science and Technology* **6**, 010501 (2025).
- [24] I. von Glehn, J. S. Spencer, and D. Pfau, [A self-attention ansatz for ab-initio quantum chemistry](#) (2023), [arXiv:2211.13672 \[physics.chem-ph\]](#).
- [25] R. Rende, S. Goldt, F. Becca, and L. L. Viteritti, Fine-tuning neural network quantum states, *Physical Review Research* **6**, [10.1103/physrevresearch.6.043280](#) (2024).
- [26] Y.-H. Zhang and M. Di Ventra, Transformer quantum state: A multipurpose model for quantum many-body problems, *Phys. Rev. B* **107**, 075147 (2023).
- [27] M. Scherbela, R. Reisenhofer, L. Gerard, P. Marquetand, and P. Grohs, Solving the electronic schrödinger equation for multiple nuclear geometries with weight-sharing deep neural networks, *Nature Computational Science* **2**, 1 (2022).
- [28] N. Gao and S. Günemann, Ab-initio potential energy surfaces by pairing GNNs with neural wave functions, in *International Conference on Learning Representations* (2022).
- [29] N. Gao and S. Günemann, Generalizing neural wave functions, in *International Conference on Machine Learning (ICML)* (2023).
- [30] J. Miao, C.-Y. Hsieh, and S.-X. Zhang, Neural-network-encoded variational quantum algorithms, *Phys. Rev. Appl.* **21**, 014053 (2024).
- [31] L. Wang, Y.-H. Liu, J. Imriška, P. N. Ma, and M. Troyer, Fidelity susceptibility made simple: A unified quantum monte carlo approach, *Phys. Rev. X* **5**, 031007 (2015).
- [32] L. Campos Venuti and P. Zanardi, Quantum critical scaling of the geometric tensors, *Phys. Rev. Lett.* **99**, 095701 (2007).
- [33] P. Zanardi, P. Giorda, and M. Cozzini, Information-theoretic differential geometry of quantum phase transitions, *Phys. Rev. Lett.* **99**, 100603 (2007).
- [34] S. Yun, M. Jeong, R. Kim, J. Kang, and H. J. Kim, Graph transformer networks, in *Advances in Neural Information Processing Systems*, Vol. 32, edited by H. Wallach, H. Larochelle, A. Beygelzimer, F. d'Alché-Buc, E. Fox, and R. Garnett (Curran Associates, Inc., 2019).
- [35] S.-J. GU, Fidelity approach to quantum phase transitions, *International Journal of Modern Physics B* **24**, 4371–4458 (2010).
- [36] J. Carrasquilla and R. G. Melko, Machine learning phases of matter, *Nature Physics* **13**, 431–434 (2017).
- [37] E. P. L. van Nieuwenburg, Y.-H. Liu, and S. D. Huber,

- Learning phase transitions by confusion, *Nature Physics* **13**, 435–439 (2017).
- [38] H.-Y. Huang, R. Kueng, and J. Preskill, Predicting many properties of a quantum system from very few measurements, *Nature Physics* **16**, 1050–1057 (2020).
- [39] H.-Y. Huang, R. Kueng, G. Torlai, V. V. Albert, and J. Preskill, Provably efficient machine learning for quantum many-body problems, *Science* **377**, 10.1126/science.abk3333 (2022).
- [40] S. Sachdev, Quantum phase transitions, *Physics world* **12**, 33 (1999).
- [41] B. Damski, Fidelity susceptibility of the quantum ising model in a transverse field: The exact solution, *Phys. Rev. E* **87**, 052131 (2013).
- [42] D. Schwandt, F. Alet, and S. Capponi, Quantum monte carlo simulations of fidelity at magnetic quantum phase transitions, *Phys. Rev. Lett.* **103**, 170501 (2009).
- [43] A. F. Albuquerque, F. Alet, C. Sire, and S. Capponi, Quantum critical scaling of fidelity susceptibility, *Phys. Rev. B* **81**, 064418 (2010).
- [44] J. J. Binney, N. J. Dowrick, A. J. Fisher, and M. Newman, *The Theory of Critical Phenomena: An Introduction to the Renormalization Group* (Oxford University Press, Inc., USA, 1992).
- [45] M. P. Gelfand, R. R. P. Singh, and D. A. Huse, Zero-temperature ordering in two-dimensional frustrated quantum heisenberg antiferromagnets, *Phys. Rev. B* **40**, 10801 (1989).
- [46] A. Moreo, E. Dagotto, T. Jolicoeur, and J. Riera, Incommensurate correlations in the t-j and frustrated spin-1/2 heisenberg models, *Phys. Rev. B* **42**, 6283 (1990).
- [47] A. Chubukov, First-order transition in frustrated quantum antiferromagnets, *Phys. Rev. B* **44**, 392 (1991).
- [48] N. Read and S. Sachdev, Large-n expansion for frustrated quantum antiferromagnets, *Phys. Rev. Lett.* **66**, 1773 (1991).
- [49] M. Mambrini, A. Läuchli, D. Poilblanc, and F. Mila, Plaquette valence-bond crystal in the frustrated heisenberg quantum antiferromagnet on the square lattice, *Phys. Rev. B* **74**, 144422 (2006).
- [50] P. Sindzingre, N. Shannon, and T. Momoi, Phase diagram of the spin-1/2 j_1 - j_2 - j_3 heisenberg model on the square lattice, *Journal of Physics: Conference Series* **200**, 022058 (2010).
- [51] W.-Y. Liu, J. Hasik, S.-S. Gong, D. Poilblanc, W.-Q. Chen, and Z.-C. Gu, Emergence of gapless quantum spin liquid from deconfined quantum critical point, *Phys. Rev. X* **12**, 031039 (2022).
- [52] W.-Y. Liu, D. Poilblanc, S.-S. Gong, W.-Q. Chen, and Z.-C. Gu, Tensor network study of the spin- $\frac{1}{2}$ square-lattice J_1 - J_2 - J_3 model: Incommensurate spiral order, mixed valence-bond solids, and multicritical points, *Phys. Rev. B* **109**, 235116 (2024).
- [53] M. Calandra Buonauro and S. Sorella, Numerical study of the two-dimensional heisenberg model using a green function monte carlo technique with a fixed number of walkers, *Phys. Rev. B* **57**, 11446 (1998).
- [54] A. W. Sandvik, Finite-size scaling of the ground-state parameters of the two-dimensional heisenberg model, *Phys. Rev. B* **56**, 11678 (1997).
- [55] L. Capriotti, F. Becca, A. Parola, and S. Sorella, Suppression of dimer correlations in the two-dimensional J_1 – J_2 heisenberg model: An exact diagonalization study, *Phys. Rev. B* **67**, 212402 (2003).
- [56] C. Lacroix, P. Mendels, and F. Mila, Introduction to frustrated magnetism, *Introduction to Frustrated Magnetism: Materials, Experiments, Theory*, Springer Series in Solid-State Sciences, Volume 164. ISBN 978-3-642-10588-3. Springer-Verlag Berlin Heidelberg, 2011 -1 (2011).
- [57] G. Parisi, Nobel lecture: Multiple equilibria, *Reviews of Modern Physics* **95**, 030501 (2023).
- [58] D. A. Abanin, E. Altman, I. Bloch, and M. Serbyn, Colloquium: Many-body localization, thermalization, and entanglement, *Reviews of Modern Physics* **91**, 021001 (2019).
- [59] P. Sierant, M. Lewenstein, A. Scardicchio, L. Vidmar, and J. Zakrzewski, Many-body localization in the age of classical computing, *Reports on Progress in Physics* **88**, 026502 (2025).
- [60] B. M. McCoy and T. T. Wu, Theory of a two-dimensional ising model with random impurities. i. thermodynamics, *Physical Review* **176**, 631 (1968).
- [61] D. S. Fisher, Random transverse field ising spin chains, *Phys. Rev. Lett.* **69**, 534 (1992).
- [62] A. P. Young and H. Rieger, Numerical study of the random transverse-field ising spin chain, *Phys. Rev. B* **53**, 8486 (1996).
- [63] C. Krämer, J. A. Koziol, A. Langheld, M. Hörmann, and K. P. Schmidt, Quantum-critical properties of the one- and two-dimensional random transverse-field ising model from large-scale quantum monte carlo simulations, *SciPost Physics* **17**, 10.21468/scipostphys.17.2.061 (2024).
- [64] T. Wolf, L. Debut, V. Sanh, J. Chaumond, C. Delangue, A. Moi, P. Cistac, T. Rault, R. Louf, M. Funtowicz, J. Davison, S. Shleifer, P. von Platen, C. Ma, Y. Jernite, J. Plu, C. Xu, T. L. Scao, S. Gugger, M. Drame, Q. Lhoest, and A. M. Rush, Transformers: State-of-the-art natural language processing, in *Proceedings of the 2020 Conference on Empirical Methods in Natural Language Processing: System Demonstrations* (Association for Computational Linguistics, Online, 2020) pp. 38–45.
- [65] F. Vicentini, D. Hofmann, A. Szabó, D. Wu, C. Roth, C. Giuliani, G. Pescia, J. Nys, V. Vargas-Calderón, N. Astrakhantsev, and G. Carleo, NetKet 3: Machine Learning Toolbox for Many-Body Quantum Systems, *SciPost Phys. Codebases* **7** (2022).
- [66] K. Choo, A. Mezzacapo, and G. Carleo, Fermionic neural-network states for ab-initio electronic structure, *Nature communications* **11**, 2368 (2020).
- [67] J. Hermann, J. Spencer, K. Choo, A. Mezzacapo, W. M. C. Foulkes, D. Pfau, G. Carleo, and F. Noé, Ab initio quantum chemistry with neural-network wavefunctions, *Nature Reviews Chemistry* **7**, 692 (2023).
- [68] M. Scherbela, L. Gerard, and P. Grohs, Towards a transferable fermionic neural wavefunction for molecules, *Nature Communications* **15**, 120 (2024).
- [69] A. Sinibaldi, D. Hendry, F. Vicentini, and G. Carleo, *Time-dependent neural galerkin method for quantum dynamics* (2024), arXiv:2412.11778 [quant-ph].
- [70] A. V. de Walle, M. Schmitt, and A. Bohrdt, *Many-body dynamics with explicitly time-dependent neural quantum states* (2024), arXiv:2412.11830 [quant-ph].
- [71] X. Yuan, S. Endo, Q. Zhao, Y. Li, and S. C. Benjamin, Theory of variational quantum simulation, *Quantum* **3**, 191 (2019).
- [72] M. Schmitt and M. Heyl, Quantum many-body dynamics in two dimensions with artificial neural networks, *Phys.*

- Rev. Lett. **125**, 100503 (2020).
- [73] J. Stokes, J. Izaac, N. Killoran, and G. Carleo, Quantum natural gradient, *Quantum* **4**, 269 (2020).
- [74] D. Wu, R. Rossi, F. Vicentini, N. Astrakhantsev, F. Becca, X. Cao, J. Carrasquilla, F. Ferrari, A. Georges, M. Hibat-Allah, M. Imada, A. M. Läuchli, G. Mazzola, A. Mezzacapo, A. Millis, J. R. Moreno, T. Neupert, Y. Nomura, J. Nys, O. Parcollet, R. Pohle, I. Romero, M. Schmid, J. M. Silvester, S. Sorella, L. F. Tocchio, L. Wang, S. R. White, A. Wietek, Q. Yang, Y. Yang, S. Zhang, and G. Carleo, Variational benchmarks for quantum many-body problems, *Science* **386**, 296 (2024), <https://www.science.org/doi/pdf/10.1126/science.adg9774>.
- [75] W.-J. Hu, F. Becca, A. Parola, and S. Sorella, Direct evidence for a gapless Z_2 spin liquid by frustrating néel antiferromagnetism, *Phys. Rev. B* **88**, 060402 (2013).
- [76] R. Coldea, D. A. Tennant, A. M. Tsvelik, and Z. Tyliczynski, Experimental realization of a 2d fractional quantum spin liquid, *Phys. Rev. Lett.* **86**, 1335 (2001).
- [77] D. Heidarian, S. Sorella, and F. Becca, Spin- $\frac{1}{2}$ heisenberg model on the anisotropic triangular lattice: From magnetism to a one-dimensional spin liquid, *Phys. Rev. B* **80**, 012404 (2009).
- [78] J. Hasik and P. Corboz, Incommensurate order with translationally invariant projected entangled-pair states: Spiral states and quantum spin liquid on the anisotropic triangular lattice, *Phys. Rev. Lett.* **133**, 176502 (2024).